Highly restricted near-surface permafrost extent during the mid-Pliocene warm period

Donglin Guo[a,b,1], Huijun Wang[b], Vladimir E. Romanovsky[c,d], Alan M. Haywood[e], Nick Pepin[f], Ulrich Salzmann[g], Jianqi Sun[a], Qing Yan[a], Zhongshi Zhang[h], Xiangyu Li[h], Bette L. Otto-Bliesner[i], Ran Feng[j], Gerrit Lohmann[k], Christian Stepanek[k], Ayako Abe-Ouchi[l], Wing-Le Chan[l], W. Richard Peltier[m], Deepak Chandan[m], Anna S. von der Heydt[n], Camille Contoux[o], Mark A. Chandler[p,q], Ning Tan[r], Qiong Zhang[s], Stephen J. Hunter[e], and Youichi Kamae[t]

Accurate understanding of permafrost dynamics is critical for evaluating and mitigating impacts that may arise as permafrost degrades in the future; however, existing projections have large uncertainties. Studies of how permafrost responded historically during Earth's past warm periods are helpful in exploring potential future permafrost behavior and to evaluate the uncertainty of future permafrost change projections. Here, we combine a surface frost index model with outputs from the second phase of the Pliocene Model Intercomparison Project to simulate the near-surface (~3 to 4 m depth) permafrost state in the Northern Hemisphere during the mid-Pliocene warm period (mPWP, ~3.264 to 3.025 Ma). This period shares similarities with the projected future climate. Constrained by proxy-based surface air temperature records, our simulations demonstrate that near-surface permafrost was highly spatially restricted during the mPWP and was 93 ± 3% smaller than the preindustrial extent. Near-surface permafrost was present only in the eastern Siberian uplands, Canadian high Arctic Archipelago, and northernmost Greenland. The simulations are similar to near-surface permafrost changes projected for the end of this century under the SSP5-8.5 scenario and provide a perspective on the potential permafrost behavior that may be expected in a warmer world.

Permafrost, that is, ground with a temperature remaining at or below 0 °C for at least two consecutive years (1), currently underlies approximately 22% of the land surface of the Northern Hemisphere (2) and stores approximately 11,000 to 37,000 km³ of ground ice (3), 1,330 to 1,580 Pg of organic carbon (4, 5), and a large pool of the harmful substance mercury (6) and various potentially harmful microorganisms (7). Both observations and model simulations indicate that permafrost will likely degrade substantially as global temperature increases (1, 8, 9). Any permafrost degradation, accompanied by melting of ground ice and release of organic carbon and harmful substances, will have considerable impacts on ecosystems (10), water resources (11), engineering infrastructure (12, 13), climate (4), and human health (7). However, the rate of projected future permafrost decline is subject to large uncertainty due to the variable climate sensitivities of climate models and differences in details of soil-related processes across different models (14–16). Thus, informed policy decisions for mitigation and adaptation are difficult.

Past Earth conditions form a useful laboratory for climate-model verification, as there is no model-independent source of information for future climate, yet model-based projections remain our only quantitative tool for research. Simulation uncertainty can be reduced through comparison of model output against available proxy-based records. To help verify models and evaluate the uncertainty of future permafrost change projections produced with these models, it is necessary to study permafrost during Earth's past (17–20). Of particular interest are past warm periods that share similarities with future conditions.

The mid-Pliocene warm period [mPWP: ~3.264 to 3.025 Ma (21)] is the most recent period of sustained (10^4-y timescales) global warmth in geological history (22). It is characterized by land–sea distribution, topography, and greenhouse gas levels similar to the present day (21, 23) and arguably represents a natural experiment from which we can gain insights about our future climate (24). Our knowledge of the mPWP has been considerably improved through coordinated model simulations (Pliocene Model Intercomparison Project, PlioMIP) (25, 26), together with proxy-based temperature reconstructions (21, 27). PlioMIP Phase 2 (PlioMIP 2) simulations predicted that the global annual mean surface air temperature was 3.2 °C higher in the mPWP than in the preindustrial period (PI) (26). In particular, the annual mean mPWP surface air temperature was 7.2 °C higher in arctic regions (28). However, this simulated arctic warming is still weaker than that obtained through proxy-based reconstructions (29).

Significance

To better understand how near-surface permafrost may respond to future warming, we explore the equilibrium spatial extent of near-surface permafrost during the mid-Pliocene warm period (mPWP), which shares characteristics of the projected future climate. Our simulations, which are constrained by proxy records, suggest highly restricted near-surface permafrost extent during the mPWP, akin to future large-scale permafrost degradation projections of our model for the end of this century. Our study indicates dramatically smaller-than-present near-surface permafrost extent in the geological past under climate conditions analogous to those expected if global warming continues unabated. This absence in permafrost will come with critical implications for the global carbon cycle, human livelihoods and infrastructures, and surface and subsurface hydrology.

Moreover, simulated winter/summer temperature and precipitation–climate variables, which arguably have the strongest impact on permafrost stability (18, 30), have been shown to be similar for the Mid-Pliocene (3.3 to 3.0 Ma) and future [as projected for 2100 and 2200 based on the representative concentration pathway (RCP) 8.5 scenario] climate for many regions (e.g., parts of the Northern Hemisphere high latitudes) (31). Some of the regions coincide with extensive current presence of permafrost (2). The similarity of both climates suggests that mPWP permafrost state has direct implications for the future permafrost behavior if relict permafrost is not considered. Thus, the study of mPWP permafrost distribution and its associated climate drivers using models and proxy data can improve our understanding of the extent, dynamics, and uncertainty of permafrost loss in a warmer future climate.

Little is known about the permafrost state in the entire Northern Hemisphere during the mPWP (5), although geological records have been examined to infer the possible formation of permafrost at a few localities during periods approaching the mPWP (32–34). Models can help to derive more spatially resolved information on mPWP permafrost. Here, we use Pliocene Model Intercomparison Project Phase 2 (PlioMIP2) climate simulations in combination with a surface frost index (SFI) model (see *permafrost diagnosis methods*) to examine the spatial pattern of near-surface [~3 to 4 m depth (35)] permafrost over the entire Northern Hemisphere during the mPWP and compare its extent to that during the PI period. Independent proxy-based temperature data are used as a constraint to evaluate the model-based results.

Results

The multimodel ensemble mean of PlioMIP2 simulations shows that the mean annual surface air temperature is 6.5 ± 2.3 °C higher during the mPWP than during the PI period in present-day permafrost regions (*SI Appendix,* Fig. S1). Compared to the PI period, the mean surface air temperature of the warmest month increases by 7.0 ± 3.4 °C, whereas that of the coldest month increases by 5.4 ± 2.5 °C. Twelve out of 17 models indicate a larger increase in the mean surface air temperature of the warmest month than of the coldest month. For the mean winter snow depth, 15 out of 17 models indicate the presence of more snow compared to the preindustrial, with an area-mean increase of 5.5 ± 4.1 cm, which is presumably due to warmer air inducing a greater supply of moisture for snowfall (36). Snow acts as a very efficient thermal insulator for the ground during winter, and consequently, it reduces the potential for the presence of permafrost (37, 38).

Forced with the PlioMIP2 climate simulations, our permafrost simulations with the SFI model demonstrate that mPWP near-surface permafrost is substantially less extensive than during the PI period (Fig. 1*B* and *SI Appendix,* Fig. S2). However, the difference in simulated mPWP near-surface permafrost extent relative to preindustrial shows a wide range (–15 to –96%) across the models, with a multimodel ensemble mean of –77% and a standard deviation (SD) of ±24% (Fig. 1*A*). The multimodel ensemble mean indicates that mPWP near-surface permafrost is present only in the eastern Siberian uplands, along the Russian Arctic coast, in the Canadian high Arctic Archipelago, and across northernmost Greenland (Fig. 1*B*).

The percentage difference in mPWP versus preindustrial near-surface permafrost area across models is significantly correlated with the annual mean surface air temperature increase in mPWP versus preindustrial (R = –0.85, *P* < 0.001) and even more with the temperature increase in the warmest month (R = –0.90, *P* < 0.001) (*SI Appendix,* Fig. S3). The percentage difference in mPWP and preindustrial near-surface permafrost extent is also closely correlated with the equilibrium climate sensitivity (ECS) (*SI Appendix,* Fig. S3*E* and Table S1) of each model (R = –0.50, *P* < 0.05). Models with higher ECS always simulate greater warming in the present-day permafrost region (*SI Appendix,* Fig. S3*F*), which in turn leads to the simulated absence of mPWP permafrost in those regions.

To reduce the large model spread in simulating mPWP permafrost change, we use proxy-based mean annual surface air temperatures at 35 sites (*SI Appendix,* Table S2) to constrain the PlioMIP2 simulations. We classify PlioMIP2 simulations based on an index, the mean bias (MB). The MB is the bias between the simulated and proxy-based surface air temperature anomalies (mPWP minus preindustrial) averaged over the 35 sites (*SI Appendix,* Table S2). It represents the level of agreement between simulations and proxy records in a spatially integrated manner. The MB is exclusively negative for all models but with a wide range from –0.9 °C (EC-Earth3-LR) to –6.6 °C (GISS-E2-1-G) (Fig. 2*A* and *SI Appendix,* Table S1). The models with smaller MB generally have higher spatial correlation coefficients against proxy-based temperature (R = 0.62, *P* < 0.01) (*SI Appendix,* Fig. S4 and Table S1). According to the MB, the PlioMIP2 simulations can be divided into three groups: 1) –3 °C<MB<0 °C, 2) –5 °C<MB<–3 °C, and (3) MB<–5 °C (Fig. 2*A*). Model group 1 has an ensemble mean MB of –1.9 °C, much smaller than those of group 2 (MB: –3.8 °C) and group 3 (MB: –5.7 °C). This finding indicates that model group 1 provides the best level of agreement between simulations and proxy records. Beyond the best fitting model group, basic patterns in the spatial structure of model-data mismatch (individual biases) are also reproduced in the other two groups: At locations of single proxy records, for all three model group ensembles, the bias is mainly negative and generally increases from low to high latitudes (Fig. 2 *B–D*).

The three model groups produce large differences in the ensemble mean extent of mPWP near-surface permafrost relative to preindustrial extent (Fig. 3). Group 1 shows a 93% smaller mPWP near-surface permafrost extent with a very small SD of ±3% across models. In that group, mPWP near-surface permafrost is present mostly in the eastern Siberian uplands, the Canadian high Arctic Archipelago and across northernmost Greenland (Fig. 3*A*). Group 2 exhibits a 69% smaller mPWP near-surface permafrost extent than preindustrial, with a higher SD of ±15% across models. The mPWP near-surface permafrost is present in the Arctic, especially in Canada and western Russia, with much less near-surface permafrost being present in the northern Tibetan Plateau and Alaska (Fig. 3*B*). Group 3 displays a 40% smaller mPWP near-surface permafrost extent than preindustrial, with a SD of ±15% across models. In that group, the absence of mPWP near-surface permafrost relative to the PI period is apparent in southern Alaska and Canada, the northern Western Siberian Plain, and Eastern Siberia/Kamchatka, whereas near-surface permafrost is present in other regions (Fig. 3*C*).

Group 1 models simulate the most realistic surface air temperature change for the mPWP compared to the PI period if the proxy records are taken as a benchmark. By extension, given the close relationship between the simulated permafrost extent and temperature, we consider that the group 1 results, particularly the substantially smaller mPWP near-surface permafrost extent (93 ± 3%), are the most reliable among the PlioMIP2 model ensembles if the state of permafrost is the subject of interest. The 93 ± 3% smaller mPWP near-surface permafrost extent found in group 1 also has a much smaller SD, indicating that the models align
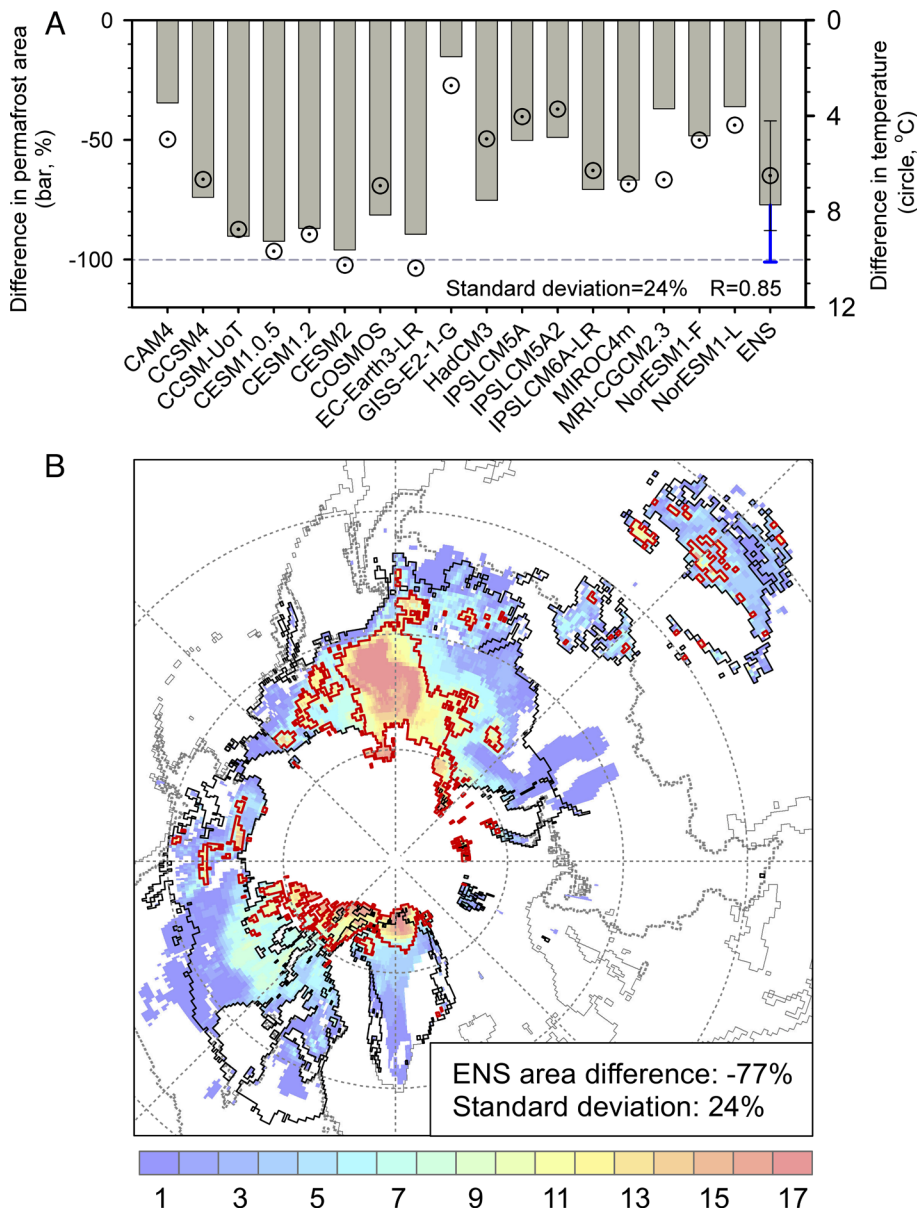
Fig. 1. Difference in near-surface permafrost between the mPWP and PI period, simulated with the SFI model driven by corrected climate data from each PlioMIP2 model and their ensemble mean (ENS). (*A*) Differences in near-surface permafrost area [*Left*, bars, %, (mPWP–PI)/PI×100] and mean annual surface air temperature (*Right*, circles, °C, mPWP–PI) averaged over the present-day permafrost region for each model and the ENS. Error bars (blue: permafrost area, black: temperature) on the ENS bar/circle indicate one standard deviation (SD) across the 17 climate models. The dashed horizontal line represents a 100% difference in permafrost area. The SD is calculated across the 17 climate models. R represents the correlation coefficient between the difference in near-surface permafrost area and the difference in mean annual temperature for each model. (*B*) Difference in near-surface permafrost extent in ENS. Areas outlined in red are the simulated near-surface permafrost extent during the mPWP, while areas outlined in black are the simulated near-surface permafrost extent during the PI. Shading denotes the differentiation of mPWP near-surface permafrost extents from the 17 models. The unit on the color bar is the total number of models that captured near-surface permafrost within the given area (red refers to more models and blue/purple refers to fewer models). ENS area difference is the percentage difference in ensemble mean near-surface permafrost area during the mPWP relative to the PI.

well. This result may be related to the uniformly smaller divergence of the group 1 models from proxy-based temperature. This smaller mPWP near-surface permafrost extent is associated with an area-averaged 9.6 ± 0.6 °C increase in mean annual surface air temperature as well as an area-averaged 5.6 ± 4.3 cm increase in mean winter snow depth in present-day permafrost regions during the mPWP relative to the PI period (*SI Appendix*, Fig. S5). During the mPWP, near-surface permafrost is found mostly in the eastern Siberian uplands, the Canadian high Arctic Archipelago, and across northernmost Greenland. The presence of near-surface permafrost is apparently related to the relatively cool surface air temperature in these regions during the mPWP (*SI Appendix*, Fig. S6A), although the temperature has significantly increased compared to that during the PI period (*SI Appendix*, Figs. S5A and *S6B*). Notably, group 1 models still have a substantial cold bias with regard to proxy records in those regions, such as in the eastern Siberian uplands. Thus, even the substantially smaller mPWP near-surface permafrost extent relative to the PI period as diagnosed by model group 1 may still slightly underestimate this difference.

Discussion

We discuss here the spatial characteristics of near-surface permafrost during the mPWP based on the PlioMIP2 simulations constrained by proxy-based surface air temperature records, i.e., the results produced by model group 1. For this group of models, mPWP near-surface permafrost is 93 ± 3% less extensive compared to the preindustrial area. Major areas of simulated mPWP near-surface permafrost are present only in the eastern Siberian uplands, Canadian high Arctic Archipelago, and northernmost Greenland.

Our simulations are compared to direct proxy data-based evidence of permafrost distribution. There is proxy data-based evidence for permafrost slightly before and after 3.26 to 3.0 Ma but none currently reported in the mPWP. The presence of ice wedge casts indicates that permafrost was likely present on Ellesmere Island in Canada's High Arctic during 3.8 to 3.63 Ma (close to but earlier than the mPWP) (39). The results from some models in group 1 are consistent with this field observation (Fig. 3A). It is thought that initial permafrost may have developed in the
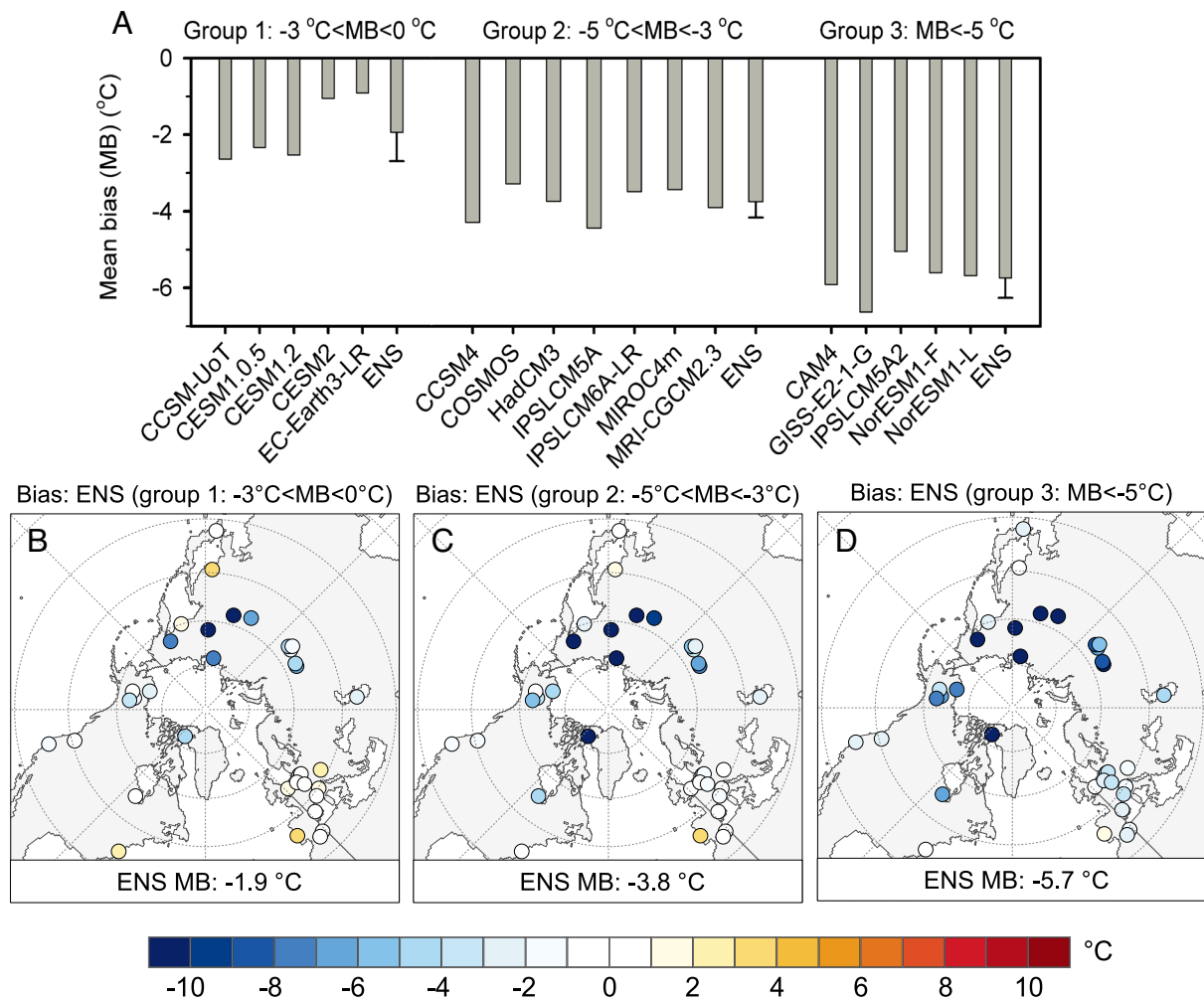
Fig. 2. Mean bias (MB, °C) of simulated mean annual temperature change during the mPWP relative to preindustrial, validated against proxy data (circles on maps) (simulation minus proxy data). (*A*) MB of the three groups of models (group 1: –3 °C<MB<0 °C, group 2: –5 °C<MB<–3 °C, and group 3: MB<–5 °C) and their ensemble mean (ENS). Error bars on ENS bars indicate one SD across the models in each group. (*B–D*) are spatial patterns of bias of the three model groups' ENS, with the ENS MB (all stations) given at the *Bottom* of each panel.

El'gygytgyn Lake region in northeastern Arctic Russia during the Pliocene Marine Isotope Stage (MIS) M2 cooling events (3.31 to 3.28 Ma), inferred based on lake sediment records (33, 40). However, the permafrost, formed during MIS M2 cooling, may have thawed in response to significant warming during the mPWP, which followed MIS M2. This appears to be consistent with the simulated absence of permafrost for the respective region as produced by model group 1 (Fig. 3*A*). In addition, permafrost was likely present in the Klondike area in western Canada by approximately 3 Ma (close to but slightly later than the mPWP), indicated by the presence of ice wedge casts (41), consistent with the results from some models in group 1. Moreover, our simulations refine the interpretation from the proxy record in that they suggest that permafrost in the Klondike area may have been only a regional phenomenon (Fig. 3*A*). The absence of permafrost is also inferred from marine fossil sediment records in northwestern Alaska during the Bigbendian marine transgression (slightly after 3 Ma, which is close to but later than the mPWP) (32), in accordance with our results (Fig. 3*A*).

Both the magnitude and spatial pattern of the near-surface permafrost extent simulated during the mPWP relative to preindustrial levels are somewhat similar to the large-scale permafrost degradation projected for the end of the 21st century under the Shared Socioeconomic Pathways (SSP) 5-8.5 scenario

(*SI Appendix*, Fig. S7*C*). We selected ten models, based on their success in simulating surface air temperature change during the 20th century (*SI Appendix*, Fig. S7*A*). They project a loss of near-surface permafrost area of 77 ± 6% in response to a surface air temperature rise of 7.5 ± 1.1 °C at the end of the 21st century under the SSP5-8.5 scenario relative to 1995 to 2014 (*SI Appendix*, Fig. S7 *B* and *C*), with near-surface permafrost remaining only in the east Siberian uplands, along the Russian Arctic coast and in the Canadian Archipelago (*SI Appendix*, Fig. S7*C*). These findings are in agreement with work presented by Slater and Lawrence (14) and Koven et al. (15), who find similar results, with losses of 81 ± 12% and 65 ± 33%, respectively, at the end of the 21st century under the RCP8.5 scenario relative to 1986 to 2005.

Notably, all these simulations, including both the future and mPWP, focus on near-surface permafrost only, which appears less resistant to climate warming than deep permafrost (42, 43). We also note that a direct comparison between mPWP permafrost extent and future permafrost loss has limitations, as it mixes the effects of greenhouse gas-related warming with those created by differences in topography. The mPWP simulations are based on a reconstructed paleotopography (21), while projections use present-day topography, and these topographical differences may contribute to the differences in both surface air temperatures and permafrost extent between the two periods. However, if we correct
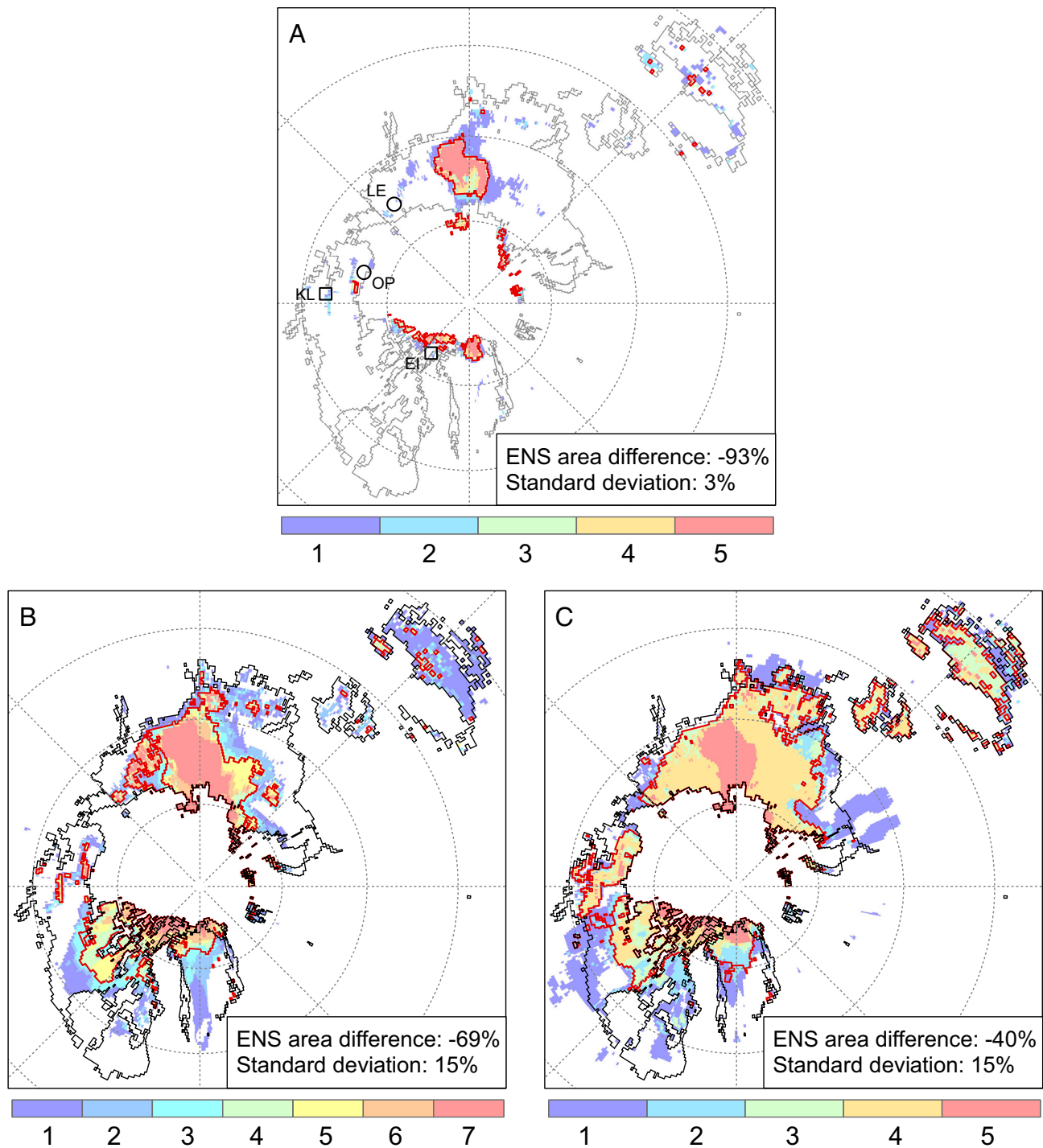
Fig. 3. Difference in near-surface permafrost extent between the mPWP and PI period, simulated with the SFI model driven by corrected climate data from the three model groups. (A–C) represent group 1: –3 °C<MB<0 °C, group 2: –5 °C<MB<–3 °C, and group 3: MB<–5 °C, respectively. Areas outlined in red show the model ensemble mean (ENS) near-surface permafrost extent during the mPWP, while areas outlined in gray (panel *A*)/black (panels *B* and *C*) illustrate the respective near-surface permafrost extent during the PI. Shading denotes the differentiation of mPWP near-surface permafrost extents derived from individual models in each group. The unit of each color bar is the total number of models that captured near-surface permafrost at that location. ENS area difference is the percentage difference in ensemble mean near-surface permafrost area during the mPWP relative to the PI. The standard deviation (SD) is calculated across all climate models within the relevant model group. In panel (*A*), the sites, where mPWP permafrost reconstruction records are available, are represented with circles and rectangles. Permafrost is assumed to be absent (present) at each site marked by a circle (rectangle). LE: Lake El'gygytgyn in northeastern Arctic Russia (39); OP: Ocean Point in northwestern Alaska (32); KL: Klondike area in western Canada (40); EI: Ellesmere Island area in Canada's High Arctic (38). Note that KL and EI represent an area surrounding the site, not just the site location because the longitudes/latitudes of site KL, provided by the literature (40), appear to be regional mean coordinates, and the longitude/latitude of EI, provided by the literature (38), is only approximate.

the simulated mPWP climate to account for present-day topography by using the assumed mean atmospheric lapse rate (–0.65 °C/100 m), then we obtain similar results on near-surface permafrost extent with regard to both the smaller extent relative to

preindustrial (94 ± 3%) and the spatial pattern of permafrost extent (*SI Appendix*, Fig. S8). This finding indicates that localized differences in topography between the mPWP and present day are not a major source of uncertainty in our conclusions.

An additional caveat in the relationship between the mPWP and future permafrost is related to our comparison including the effects of differences in vegetation and surficial geology (e.g., grain size of soil). The mPWP simulations take vegetation change between the mPWP and PI period into account (23, 44), whereas most of the models employed for future projections do not consider vegetation change between the future and present day (45). Exclusion of vegetation change in the models used for future projections could cause polar amplification (associated with greening) to be underestimated (46). Surficial geology has been altered since the mPWP by erosion and land-forming processes that resulted from the sequence of Quaternary glacial-interglacial cycles (47), and thus, it could have a different climatic effect during the future compared with the mPWP (48).

Besides, the comparison of permafrost must also acknowledge the effects of the difference between mPWP equilibrium and future SSP transient climate experiments. The SFI model assumes permafrost in equilibrium with a stationary climate, so permafrost may be in an equilibrium state in the mPWP experiment. Although the 20-y mean of climate data is used to address the stationarity of climate (14), the timescale may require longer for future permafrost to equilibrate given the thermal resilience of permafrost. Previous speleothem and stratigraphic studies show that even near-surface permafrost persisted, although locally, through past interglacials with multiple millennia of warmer-than-present climate, e.g., the early Holocene (49), MIS 5e (50, 51), and MIS 11 (52–55). However, despite these intrinsic differences, the mPWP remains one of the best geological analogs for the future due to both general features of Earth surface characteristics and carbon dioxide forcing being comparable to today (26, 31). Consequently, the mPWP provides a laboratory to study the dynamics and extent of permafrost in a warmer-than-present climate that may, in many aspects, be similar to future conditions (31).

Based on the success in simulating the present-day permafrost distribution (see *evaluation of permafrost diagnosis methods*), this study used the indirect SFI model diagnostic method to investigate the permafrost state during the mPWP, leading to the results discussed above. To assess whether our results depend on the type of permafrost diagnosis method employed, we also consider a direct soil temperature diagnosis. We compare the results derived from the two methods based on climate data and soil temperature data from the same four climate models (CESM2, CESM1.2, CESM1.0.5, and CCSM-UoT) in group 1. These climate models provide reasonable performance in capturing the present-day permafrost distribution (*SI Appendix,* Fig. S9). When using the direct method, we find that mPWP near-surface permafrost is 86 to 99% less extensive than during the PI period (*SI Appendix,* Fig. S10A) due to significantly higher mPWP soil temperature, particularly from June to August (*SI Appendix,* Fig. S10C). The extent of deeper mPWP permafrost is slightly greater than that of near-surface mPWP permafrost (*SI Appendix,* Fig. S10B). The relative difference between mPWP and preindustrial is similar in magnitude to that found when employing the indirect SFI model diagnostic method (mPWP near-surface permafrost extent is 87 to 96% smaller than preindustrial for models of group 1) (*SI Appendix,* Table S1), indicating that our results are not highly dependent on the permafrost diagnostic method.

Uncertainties in our SFI simulations are mostly caused by uncertainties in model boundary conditions (21) and uncertainties in model physics (26). Furthermore, the coarse resolution of some of the climate models used (e.g., NorESM1-L, 3.75° × 3.75°) provides less regional detail and limits particularly the ability to produce realistic and detailed climatic conditions at the edges of permafrost regions. An additional source of uncertainty is related to the poor proxy data coverage in some high latitude regions and uncertainty ranges of proxy data-based temperature estimates. However, as the majority (n = 21) of our selected paleosites are located north of 50°N and the overall uncertainty ranges of temperature estimates are below ±2 °C (*SI Appendix,* Table S2), it is unlikely that proxy data uncertainties have a major impact on the ranking order of our three model groups (Fig. 2) (see *proxy data-based surface air temperature data*).

The indirect SFI model diagnostic method does not consider vegetation, organic matter, and excess ground ice in surface/subsurface characteristics. Increases in vegetation cover and height generally warm soil by increasing snow depth in winter, and cool soil by increasing evapotranspiration and surface shading in summer (37, 56, 57). Soil organic matter can reduce the annual mean soil temperature and decrease the active layer thickness (42, 58). Excess ground ice can retard the thawing of near-surface permafrost due to latent heat effects (16, 38, 59). However, given the lack of sufficiently detailed information on the surface and soil characteristics of the mPWP, it is not yet possible to robustly examine these impacts. More work needs to quantify the distribution of mPWP vegetation and other permafrost-relevant land surface conditions, further exploring their impact on the simulation of near-surface permafrost during the mPWP.

Despite these uncertainties, our work provides an important step in characterizing the extent of mPWP permafrost and relating its spatial distribution to climatic and permafrost changes that are expected for the coming decades to centuries based on projections of future climate. Beyond providing a quantitative and self-consistent analysis of mPWP permafrost in comparison to today based on recent PlioMIP2 model output, our work also allows verification of permafrost simulations by means of model-independent proxy records. We illustrate links between mPWP and potential future climate based on similarities of both climate states, indicating that mPWP permafrost has direct implications for the state and stability of future permafrost. Based on our findings, the future of Northern Hemisphere near-surface permafrost appears bleak. Continued climate warming and related near-surface permafrost degradation may cause changes in ambient and environmental conditions (7, 11, 13, 60, 61) that humans have not yet experienced, implying an imperative to further highlight the importance of permafrost degradation. Our study also shows that the response of permafrost to past sustained warmth is valuable for understanding of permafrost degradation and associated climate, ecological, and societal impacts in our warming world.

Methods

mPWP and Preindustrial Climate Simulation Data for Permafrost Simulation. mPWP and preindustrial climate data were obtained from 16 coupled atmosphere-ocean climate models (AOGCM) in the PlioMIP2 (26) and an atmosphere-only climate model (AGCM) from Yan et al. (62). Key details of these models are shown in *SI Appendix,* Table S1. All 17 models provide monthly surface air temperature (2 m) and precipitation (used to calculate snow depth). These data are employed to drive the SFI model, with a snow density assumption of 250 kg m^{-3} according to Slater and Lawrence (14). For 8 of the 17 models (CESM2, CESM1.2, CESM1.0.5, CCSM4, CCSM-UoT, EC-Earth3-LR, GISS-E2-1-G, and IPSLCM6A-LR), monthly soil temperatures were available and used to directly diagnose permafrost distribution (the SFI model was not used in this case). In addition, monthly snow depth and snow mass (used to calculate snow density) were also available for CESM2 and were used to drive the SFI model in combination with monthly surface air temperature. Compared to PlioMIP1, PlioMIP2 simulations are underpinned by state-of-the-art boundary conditions (e.g., updated paleogeographic reconstructions detailing ocean bathymetry, land ice surface topography, and updated Pliocene soil and lake distribution datasets) from the

latest Pliocene Research-Interpretation and Synoptic Mapping version 4 (21). Sea ice is predicted dynamically by the climate models. The Arctic is nearly sea ice free in summer but covered by substantial amounts of sea ice in winter during the mPWP as indicated by the majority of the models (28). Additional details regarding the mPWP simulation setup can be found in Haywood et al. (23). All but two of the AOGCMs have produced simulations with a length in excess of 1,000 model years for both mPWP and preindustrial experiments (26). The final 100 y of each simulation are analyzed in this study. In the case of the AGCM, the simulation ran for a length of 10 (7) y for mPWP (preindustrial), respectively (62), and the final 5 y of results are analyzed. Data for the models CESM2, EC-Earth3-LR, GISS-E2-1-G, IPSL-CM6A-LR, and NorESM1-F are archived at the Earth System Grid Federation (ESGF) gateway (https://esgf-node.llnl.gov/). Data from other models have been provided by the corresponding modeling groups (26, 62).

CRU Climate Data. Observed monthly surface air temperature and precipitation (used to calculate snow depth) are obtained from CRU TS 4.04 data at a spatial resolution of 0.5° × 0.5° available at https://crudata.uea.ac.uk/cru/data/hrg/cru_ts_4.04/. These data are used to drive the SFI model to diagnose preindustrial permafrost and to correct simulated climate data from PlioMIP2. The dataset covers the time period of 1901 to 2019. In the absence of CRU TS 4.04 data for 1850, we used the years 1901 to 1930 to represent the PI period. This choice is justified because the state of the climate does not substantially change over these periods (63). CRU TS 4.04 is a gridded dataset that is produced from station observations. Station anomalies are first interpolated to a high-resolution grid and then added to an existing climatology to yield absolute values. More details can be found in Harris et al. (64). CRU is an established dataset and has been used worldwide for research on climate change detection (65–67).

International Permafrost Association (IPA) Map. The IPA map (68) is used as a source of observations to validate our permafrost simulations for the PI period. Because the map is produced using data from 1960 to 1993 (68) while the PI period refers to 1850, there is an unavoidable period mismatch in this validation. However, at least in Eastern Siberia, the time range from 1901 to 1960 does not appear to be an example of continuous permafrost degradation but rather was characterized by intermittent periods of increases and reductions in active layer thickness (69). This finding provides some confidence that the IPA map may be suitable to provide estimates of large-scale patterns of permafrost as present during the earlier part of the 20th century and, by extension, during the PI period. The map discriminates permafrost into continuous, discontinuous, sporadic, and isolated types. Given that the simulation at a resolution of 0.5° × 0.5° may identify only continuous and discontinuous permafrost (16), we limited the validation of our simulations to areas of continuous and discontinuous permafrost. The permafrost data are available at https://nsidc.org/data/GGD318/versions/2 and are considered to be one of the best available sources on permafrost distribution (14).

Proxy Data-Based Surface Air Temperature Data. We used quantitative climate estimates from the late Pliocene (~3.6 to 2.6 Ma) paleobotanical dataset (44), which has been updated for assessing model experiments of the PlioMIP2 (29). Updates refer to additional quantitative climate estimates and uncertainty assessments, including confidence levels for each site. To reduce the risk of a potential methodological bias, we used Late Pliocene temperature estimates that were derived from the paleobotanical record (i.e., fossil pollen, leaves, and wood) using a range of different quantitative and semiquantitative methods, including bioclimatic ranges of nearest living relatives, oxygen isotopes of fossil wood, or the physiognomy of fossil leaves. The uncertainty is provided for each mean annual temperature estimate (*SI Appendix*, Table S2). Temperature estimates based on nearest living relative approaches generally include a bioclimatic range in which all taxa of the reconstructed paleovegetation can coexist. In addition, we also provide, where available, the temporal variability, which indicates the variability in the reconstructed temperature over the time period covered by the fossil record (e.g. orbitally controlled cold and warm cycles). Qualitative confidence (very high, high, medium, and low) of temperature estimates at each site is assessed based on (a) age control, (b) resolution, (c) fossil preservation, and (d) the estimation method, whereby age control and estimation method were treated as the most important criteria (*SI Appendix*, Table S2) (29). Although estimates with a high confidence level might be more reliable than those with lower confidence, differences in confidence level appear to have a rather low impact on our data-model

comparison. There is good consistency between temperature estimates derived from high- versus lower-confidence sites, particularly in high-latitude Northeast Asia and North America (29).

Proxy-based mean annual surface air temperature data from 35 sites were selected for this study to constrain the PlioMIP2 simulations. Key details of these sites are shown in *SI Appendix*, Table S2. Site choices exclude 1) sites with modern altitudes above 1,000 m due to large uncertainties in estimating Pliocene paleoaltitudes, 2) marine sites, and 3) tropical terrestrial sites with latitudes below 20°N (near the southern limit of Northern Hemisphere permafrost) due to their small representation within the permafrost region in the Northern Hemisphere. The selected sites show good spatial coverage across latitudes (Fig. 2), allowing a comprehensive data-model comparison. Data coverage is poor in the high latitudes of western Siberia, eastern Scandinavia, and the boreal zone of central North America. However, the majority (n = 21) of our selected sites are located north of 50°N, providing a good benchmark for evaluating the ability of climate models to simulate high-latitude climates in the permafrost zone.

We use the temperature midpoints of our proxy estimates as a benchmark to test the PlioMIP2 model performance and then rank the model according to the MB, assuming that the distribution of possible temperature values is concentrated near the center of the temporal and bioclimatic ranges (e.g., assuming a normal distribution) (29). All the models consistently show a cold MB, with the least cold MB being –0.9 °C for EC-Earth3-LR (Fig. 2 and *SI Appendix*, Table S1). Moreover, most of the data uncertainty ranges are below ±2.0 °C (*SI Appendix*, Table S2). Therefore, it appears unlikely that the uncertainty ranges profoundly affect the ranking order of our 3 model groups (Fig. 2). However, the uncertainty could alter the thresholds of the classification (i.e., 0 °C, –3 °C, and –5 °C for the midpoints of our proxy estimates). Proxy-based temperature anomalies are calculated as individual site records minus the nearest grid cell-mean CRU surface air temperature during 1901 to 1930, while the simulated temperature anomaly is calculated as mPWP minus preindustrial temperature at any model grid cell.

Our proxy data-model comparison is based on comparing simulated grid cell-mean surface air temperature anomalies with individual site proxy-based surface air temperature anomalies; thus, it includes a scale mismatch. This mismatch may cause uncertainties, especially in areas of complex relief. However, such uncertainties are considered to be small in this study. Most of our paleobotanical sites have elevations below 350 m, and sites that today are located above 1,000 m are explicitly excluded from the data-model comparison. In addition, the majority of our temperature estimates have been derived from palynological records that reflect pollen influx from the regional dominant vegetation communities. Consequently, the respective temperature estimates relate to a wider catchment area than the specific proxy location. Therefore, reconstructed temperatures are representative of a high proportion of the simulated grid cell (29). Beyond our study, these proxy temperature records have already been used to evaluate the ability of models from the PlioMIP1 to simulate climate during the mPWP (29).

Permafrost Diagnosis Methods. Two methods were used to diagnose permafrost: 1) the indirect permafrost model method, and 2) the direct AOGCM-modeled soil temperature method.

For the indirect permafrost model diagnostic method, the SFI model was used to estimate the near–surface permafrost extent (70):

$$SFI = \frac{\sqrt{DDF^*}}{\sqrt{DDF^*} + \sqrt{DDT}}, \qquad [1]$$

where DDF is the sum of freezing degree days. The label "*" denotes an incorporation of snow insulation effects that results in a decrease in the DDF (70). DDT is the sum of thawing degree days. For specific equations, see supplementary information (Equation set for the SFI model). The SFI values vary from 0 to 1. If SFI > 0.6, then either discontinuous or continuous permafrost was assumed. Model input requires four climate elements: surface air temperature in the warmest and coldest months as well as mean winter snow depth and snow density (the latter two to incorporate snow insulation effects). Surface air temperatures in the warmest and coldest months were derived from simulated monthly surface air temperature data. The mean winter snow depth is calculated using monthly

precipitation (see below), and the mean winter snow density is fixed at 250 kg m^{-3} (14).

The mean winter snow depth was calculated as (70)

$$\bar{Z}_s = \sin^2 \phi \left\{ \sum_{i=1}^{k} \left[(P_i/\rho_r)(k-(i-1)) \right] / k \right\}, \qquad [2]$$

where $\bar{Z}_s$ is the mean winter snow depth, and P_i is the precipitation in the i_{th} month ($i = 1, 2, …, k$) when the mean surface air temperature is ≤0 °C. ρ_r is snow density [250 kg m^{-3} (14)]. ϕ is the latitude. This method weights snowfall by the time of its occurrence (earlier winter snowfall has greater weighting than later spring snowfall) and considers the fact that the magnitude and duration of snow thaw varies with solar forcing (which is dependent on latitude).

The SFI model represents the importance of temperature in permafrost formation and considers any snow insulation effect but does not use information about the surface state (topography, vegetation, etc.). It indicates sustainability of the upper [near-surface, ~3 to 4 m depth (35)] permafrost layer under stationary climate conditions. While climate stationarity is implicitly assumed, it is appropriate for this study to examine the permafrost state in two stabilized scenarios: the mPWP and the preindustrial. The SFI model requires readily available input climate data and is characterized by ease of application and rapid computation, allowing us to explore permafrost change at various temporal and spatial scales. Slater and Lawrence (14) indicated that more information regarding permafrost change can be provided by the SFI model than is available via raw diagnostics using soil temperature from climate models (14).

For the direct AOGCM-modeled soil temperature diagnostic method, the following assumption is made: If there is at least one soil layer in the upper 3.5 m soil in which the monthly soil temperature remains below 0 °C for 24 consecutive months, then the respective grid cell is identified as containing near-surface permafrost (71–74). This method is used for CESM2, CESM1.2, CESM1.0.5, CCSM4, CCSM-UoT, and IPSLCM6A-LR because soil temperatures are available for these models. Although soil temperatures for EC-Earth3-LR and GISS-E2-1-G are also available, we excluded them from our analyses due to a shallow soil column (<3.0 m). All soil temperature data were interpolated to a common horizontal resolution of 0.9° × 1.25° and to a vertical resolution of 0.1 m for comparison.

Evaluation of Permafrost Diagnosis Methods. To decrease uncertainties in permafrost simulations, the two aforementioned permafrost diagnosis methods were evaluated based on the IPA map to select the optimal method for the present study. Based on the direct soil temperature method (raw AOGCM), CESM2, CESM1.2, CESM1.0.5, CCSM4, and CCSM-UoT show similar absolute biases, apparently smaller than that of IPSLCM6A-LR (*SI Appendix*, Fig. S9). Since only CESM2 provides snow depth and snow mass data, it is used to further evaluate the diagnosis methods. The absolute bias of CESM2 using soil temperatures (*SI Appendix*, Fig. S11*A*) is larger than that using the indirect SFI diagnostic method driven by 1) CESM2 surface air temperature and direct snow depth/mass (*SI Appendix*, Fig. S11*B*), 2) CESM2 surface air temperature and precipitation-calculated snow depth (*SI Appendix*, Fig. S11*C*), and 3) coarse resolution CRU surface air temperature and precipitation-calculated snow depth (resampled to CESM grid cells, 0.9° × 1.25°) (*SI Appendix*, Fig. S11*D*). This finding indicates that the indirect SFI model can capture the present-day permafrost distribution more reasonably than direct soil temperatures. The coarse-resolution CRU surface air temperature and precipitation-calculated snow depth yield the least absolute bias (*SI Appendix*, Fig. S11 *B–D*). In addition, high-resolution (0.5° × 0.5°) CRU surface air temperature and precipitation-calculated snow depth-based results provide more regional details (*SI Appendix*, Fig. S12), although the derived permafrost area has a somewhat larger absolute bias (5.2 × 10^6 km^2) (*SI Appendix*, Fig. S12) than that based on the coarse-resolution (CESM grid cell) method (4.6 × 10^6 km^2) (*SI Appendix*, Fig. S11*D*).

As shown in *SI Appendix*, Fig. S12, the permafrost extent computed based on the high-resolution CRU surface air temperature and precipitation-calculated snow depth broadly resembles the IPA map, despite an overestimation in the Labradorean region in northeastern Canada and on the eastern Tibetan Plateau and a slight underestimation in southern Alaska and in the northern part of the Western Siberian Plain. Based on this sensitivity analysis, our study employs the indirect SFI model method driven by high-resolution CRU surface air temperature

and precipitation-calculated snow depth to obtain near-surface permafrost distribution during the PI period.

Simulation of near-surface Permafrost during the mPWP. For the mPWP permafrost simulation, we first correct systematic biases in the simulated mPWP climate data using the anomaly method. Specifically, the simulated mPWP climate anomaly is added to the present-day observed climatology, i.e., high-resolution CRU climatology (1901 to 1930). The anomaly of surface air temperature denotes the absolute temperature change between the mPWP and PI period, while the anomaly of snow depth denotes a percentage change in snow depth. Then, the corrected climate data are used to drive the SFI model to obtain the permafrost distribution during the mPWP. For comparison, we also analyze the mPWP permafrost distribution obtained with the SFI model driven by raw climate data (i.e., without correcting any systematic biases) from the three model groups (*SI Appendix*, Fig. S13). The permafrost distributions based on raw climate data are similar overall to those based on corrected climate data (*SI Appendix*, Fig. S13 and Fig. 3). Simulations based on raw climate data illustrate slightly smaller permafrost extent during the mPWP than those based on corrected climate data. In addition, raw climate data appear to simulate a larger mPWP permafrost extent in Canada and the Tibetan Plateau but a smaller extent in Russia (*SI Appendix*, Fig. S13). This finding corresponds to cooler temperatures in Canada and the Tibetan Plateau and warmer temperatures in Russia (eastern Siberian uplands) in raw climate data (*SI Appendix*, Fig. S14) relative to corrected data (*SI Appendix*, Fig. S6).

Permafrost Projection Method. We use simulated historical (1901 to 2014) and future (2015 to 2100, SSP5-8.5 scenario) climate data from 22 models participating in the sixth phase of the Coupled Model Intercomparison Project (CMIP6). The climate datasets provided by all models include monthly surface air temperature and precipitation (used to calculate snow depth). The characteristics of the CMIP6 models considered here are shown in *SI Appendix*, Table S3 together with basic model-derived temperature and permafrost statistics. Details regarding the design of the CMIP6 simulations can be found in Eyring et al. (45). The climate model datasets employed here have been retrieved from the ESGF (https://esgf-node.llnl.gov/).

Similar to the mPWP permafrost simulation, we use the anomaly method to correct systematic biases in simulated historical and future climate data. The anomaly of each simulated climate variable is first calculated relative to the period of 1995 to 2014 and then added to the present-day (1995 to 2014) high-resolution CRU climatology to derive the climate forcing for the permafrost simulation. Given the implicit assumption of climatic stationarity in the SFI model, corrected climate data are averaged using a 20-y sliding window (14). Near-surface permafrost distributions for both the end of the 21st century and the present-day are simulated using the SFI model, which is driven by the 20-y averages of corrected climate data over the periods of 2080 to 2099 and 1995 to 2014, respectively. The difference between the two simulated permafrost distributions indicates future change in near-surface permafrost during the end of the 21st century relative to the present day.

In addition, we constrain the 22 CMIP6 models for the present day using the MB between the simulated and CRU surface air temperature anomalies (1995 to 2014 minus 1901 to 1930) averaged over the present-day permafrost region. As a result, 10 preferred models are chosen due to their small MBs (–0.3 °C < MB < 0.3 °C) (*SI Appendix*, Fig. S7*A* and Table S3). The permafrost projections produced by these 10 preferred models are the focus of most of the analyses of present-day/future permafrost changes (*SI Appendix*, Fig. S7).

Data, Materials, and Software Availability. All study data are included in the article and/or *SI Appendix*.

Author affiliations: ᵃNansen-Zhu International Research Centre, Institute of Atmospheric Physics, Chinese Academy of Sciences, Beijing 100029, China; ᵇKey Laboratory of Meteorological Disaster, Ministry of Education/Collaborative Innovation Center on Forecast and Evaluation of Meteorological Disasters, Nanjing University of Information Science and Technology, Nanjing 210044, China; ᶜGeophysical Institute, University of Alaska Fairbanks, Fairbanks, AK 99775; ᵈEarth Cryosphere Institute, Tyumen Scientific Centre, Siberian Branch of the Russian Academy of Science, Tyumen 625026, Russia; ᵉSchool of Earth and Environment, University of Leeds, Leeds LS2 9JT, United Kingdom; ᶠSchool of Environment, Geography and Geosciences, University of Portsmouth, Portsmouth PO1 3HE, United Kingdom; ᵍDepartment of Geography and Environmental Sciences, Northumbria University, Newcastle upon Tyne NE1 8ST, United Kingdom; ʰDepartment of Atmospheric Science, School of Environmental Studies, China University of Geoscience, Wuhan 430074, China; ⁱClimate and Global Dynamics Laboratory, National Center for Atmospheric Research, Boulder, CO 80307; ʲDepartment of Earth Sciences, University of Connecticut, Storrs, CT 06269; ᵏAlfred Wegener Institute, Helmholtz Centre for Polar and Marine Research, Bremerhaven 27570, Germany; ˡAtmosphere and Ocean Research Institute, University of Tokyo, Kashiwa 277-8568, Japan; ᵐDepartment of Physics, University of Toronto, Toronto M5S 1A7, Canada; ⁿInstitute for Marine and Atmospheric Research Utrecht, Department of Physics, Utrecht University, Utrecht 3584 CC, The Netherlands; ᵒLaboratoire des Sciences du Climat et de l'Environnement/Institut Pierre Simon Laplace, Commissariat à l'Energie Atomique-Centre National de la Recherche Scientifique-Université de Versailles Saint Quentin, Université Paris-Saclay, Gif-sur-Yvette 91191, France; ᵖCenter for Climate Systems Research, Columbia University, New York, NY 10025; �q Goddard Institute for Space Studies, National Aeronautics and Space Administration, New York, NY 10025; ʳKey Laboratory of Cenozoic Geology and Environment, Institute of Geology and Geophysics, Chinese Academy of Sciences, Beijing 100029, China; ˢDepartment of Physical Geography and Bolin Centre for Climate Research, Stockholm University, Stockholm 10691, Sweden; and ᵗFaculty of Life and Environmental Sciences, University of Tsukuba, Tsukuba 305-8572, Japan

1. B. Biskaborn et al., Permafrost is warming at a global scale. Nat. Commun. 10, 264 (2019).
2. Y. Obu et al., Northern Hemisphere permafrost map based on TTOP modelling for 2000–2016 at 1 km² scale. Earth Sci. Rev. 193, 299–316 (2019).
3. T. Zhang, R. Barry, K. Knowles, J. Heginbottom, J. Brown, Statistics and characteristic of permafrost and ground-ice distribution in the Northern Hemisphere. Polar Geogr. 31, 47–68 (2008).
4. E. Schuur et al., Climate change and the permafrost carbon feedback. Nature 520, 171–179 (2015).
5. K. Miner et al., Permafrost carbon emissions in a changing Arctic. Nat. Rev. Earth Environ. 3, 55–67 (2022).
6. P. Schuster et al., Permafrost stores a globally significant amount of mercury. Geophys. Res. Lett. 45, 1463–1471 (2018).
7. J. D'Costa et al., Antibiotic resistance is ancient. Nature 477, 457–461 (2011).
8. J. Aalto, S. Harrison, M. Luoto, Statistical modelling predicts almost complete loss of major periglacial processes in Northern Europe by 2100. Nat. Commun. 8, 515 (2017).
9. S. Chadburn et al., An observation-based constraint on permafrost loss as a function of global warming. Nat. Clim. Change 7, 340–344 (2017).
10. J. Vonk et al., Reviews and syntheses: Effects of permafrost thaw on Arctic aquatic ecosystems. Biogeosciences 12, 7129–7167 (2015).
11. A. Liljedahl et al., Pan-Arctic ice-wedge degradation in warming permafrost and its influence on tundra hydrology. Nat. Geosci. 9, 312–318 (2016).
12. J. Hjort et al., Degrading permafrost puts Arctic infrastructure at risk by midcentury. Nat. Commun. 9, 5147 (2018).
13. J. Hjort et al., Impacts of permafrost degradation on infrastructure. Nat. Rev. Earth Environ. 3, 24–38 (2022).
14. A. Slater, D. Lawrence, Diagnosing present and future permafrost from climate models. J. Clim. 26, 5608–5623 (2013).
15. C. Koven, W. Riley, A. Stern, Analysis of permafrost thermal dynamics and response to climate change in the CMIP5 Earth system models. J. Clim. 26, 1877–1900 (2013).
16. C. Burn, F. Nelson, Comment on "A projection of severe near-surface permafrost degradation during the 21st century" by David M. Lawrence and Andrew G. Slater. Geophys. Res. Lett. 33, L21503 (2006).
17. J. Tierney et al., Past climates inform our future. Science 370, eaay3701 (2020).
18. S. Smith, H. O'Neill, K. Isaksen, J. Noetzli, V. Romanovsky, The changing thermal state of permafrost. Nat. Rev. Earth Environ. 3, 10–23 (2022).
19. K. Saito et al., LGM permafrost distribution: How well can the latest PMIP multi-model ensembles perform reconstruction? Clim. Past 9, 1697–1714 (2013).
20. Y. Liu, D. Jiang, Mid-Holocene permafrost: Results from CMIP5 simulations. J. Geophys. Res. Atmos. 121, 221–240 (2016).
21. H. Dowsett et al., The PRISM4 (mid-Piacenzian) paleoenvironmental reconstruction. Clim. Past 12, 1519–1538 (2016).
22. A. Haywood, H. Dowsett, A. Dolan, Integrating geological archives and climate models for the mid-Pliocene warm period. Nat. Commun. 7, 10646 (2016).
23. A. Haywood et al., The Pliocene Model Intercomparison Project (PlioMIP) phase 2: Scientific objectives and experimental design. Clim. Past 12, 663–675 (2016).
24. H. Dowsett et al., Sea surface temperature of the mid-Piacenzian ocean: A data-model comparison. Sci. Rep. 3, 2013 (2013).
25. A. Haywood et al., Large-scale features of Pliocene climate: Results from the Pliocene model intercomparison project. Clim. Past 9, 191–209 (2013).
26. A. Haywood et al., The Pliocene model intercomparison project phase 2: Large-scale climate features and climate sensitivity. Clim. Past 16, 2095–2123 (2020).
27. H. Dowsett et al., Joint investigations of the Middle Pliocene climate I: PRISM paleoenvironmental reconstructions. Glob. Planet. Change 9, 169–195 (1994).
28. W. de Nooijer et al., Evaluation of Arctic warming in mid-Pliocene climate simulations. Clim. Past 16, 2325–2341 (2020).
29. U. Salzmann et al., Challenges in quantifying Pliocene terrestrial warming revealed by data–model discord. Nat. Clim. Change 3, 969–974 (2013).
30. D. Guo, J. Sun, H. Li, T. Zhang, V. Romanovsky, Attribution of historical near-surface permafrost degradation to anthropogenic greenhouse gas warming. Environ. Res. Lett. 15, 084040 (2020).
31. R. Burke et al., Pliocene and Eocene provide best analogs for near future climates. Proc. Nat. Acad. Sci. U.S.A. 115, 13288–13293 (2018).
32. L. Carter, J. Brigham-Grette, L. Marincovich, V. Jr Pease, J. Hillhouse, Late Cenozoic Arctic Ocean sea ice and terrestrial paleoclimate. Geology 14, 675–678 (1986).
33. V. Wennrich et al., Impact processes, permafrost dynamics, and climate and environmental variability in the terrestrial Arctic as inferred from the unique 3.6 Myr record of Lake El'gygytgyn, Far East Russia-A review. Quat. Sci. Rev. 147, 221–244 (2016).
34. J. Murton, What and where are periglacial landscapes? Permafrost Periglac. Process. 32, 186–212 (2021).
35. IPCC, "Summary for policymakers" in IPCC Special Report on the Ocean and Cryosphere in a Changing Climate, H. Pörtner et al., Eds. (Cambridge University Press, Cambridge, UK and New York, NY, 2019), pp. 3–35.
36. X. Zhong et al., Spatiotemporal variability of snow depth across the Eurasian continent from 1966 to 2012. Cryosphere 12, 227–245 (2018).
37. F. Domine et al., Permafrost cooled in winter by thermal bridging through snow-covered shrub branches. Nat. Geosci. 15, 554–560 (2022).
38. L. Farquharson, V. Romanovsky, A. Kholodov, D. Nicolsky, Sub-aerial talik formation observed across the discontinuous permafrost zone of Alaska. Nat. Geosci. 15, 475–481 (2022).
39. N. Rybczynski et al., Mid-Pliocene warm-period deposits in the High Arctic yield insight into camel evolution. Nat. Commun. 4, 1550 (2013).
40. V. Wennrich et al., Pliocene to Pleistocene climate and environmental history of Lake El'gygytgyn, Far East Russian Arctic, based on high-resolution inorganic geochemistry data. Clim. Past 10, 1381–1399 (2014).
41. D. Froese, R. Barendregt, R. Enkin, J. Baker, Paleomagnetic evidence for multiple late Pliocene-Early Pleistocene glaciations in the Klondike area, Yukon territory. Can. J. Earth Sci. 37, 863–877 (2000).
42. D. Lawrence, A. Slater, V. Romanovsky, D. Nicolsky, Sensitivity of a model projection of near-surface permafrost degradation to soil column depth and representation of soil organic matter. J. Geophys. Res. 113, F02011 (2008).
43. D. Nicolsky, V. Romanovsky, Modeling long-term permafrost degradation. J. Geophys. Res. Earth Surf. 123, 1756–1771 (2018).
44. U. Salzmann, A. Haywood, D. Lunt, P. Valdes, D. Hill, A new global biome reconstruction and data-model comparison for the Middle Pliocene. Global Ecol. Biogeogr. 17, 432–447 (2008).
45. V. Eyring et al., Overview of the coupled model intercomparison project phase 6 (CMIP6) experimental design and organization. Geosci. Model Dev. 9, 1937–1958 (2016).
46. R. O'ishi, A. Abe-Ouchi, Influence of dynamic vegetation on climate change arising from increasing CO2. Clim. Dyn. 33, 645–663 (2009).
47. M. Batchelor et al., The configuration of Northern Hemisphere ice sheets through the quaternary. Nat. Commun. 10, 3713 (2019).
48. M. Pound et al., Late Pliocene lakes and soils: A global data set for the analysis of climate feedbacks in a warmer world. Clim. Past 10, 167–180 (2014).
49. C. Burn, Cryostratigraphy, paleogeography, and climate change during the early Holocene warm interval, western Arctic coast, Canada. Can. J. Earth Sci. 34, 912–925 (1997).
50. A. Reyes, D. Froese, B. Jensen, Permafrost response to last interglacial warming: Field evidence from non-glaciated Yukon and Alaska. Quat. Sci. Rev. 29, 3256–3274 (2010).
51. K. Ashastina, L. Schirrmeister, M. Fuchs, F. Kienast, Palaeoclimate characteristics in interior Siberia of MIS 6–2: First insights from the Batagay permafrost mega-thaw slump in the Yana Highlands. Clim. Past 13, 795–818 (2017).
52. D. Froese, J. Westgate, A. Reyes, R. Enkin, S. Preece, Ancient permafrost and a future, Warmer Arctic. Science 321, 1648 (2008).
53. N. Biller-Celander et al., Increasing Pleistocene permafrost persistence and carbon cycle conundrums inferred from Canadian speleothems. Sci. Adv. 7, eabe5799 (2021).
54. J. Murton et al., A multimethod dating study of ancient permafrost, Batagay megaslump, east Siberia. Quat. Res. 105, 1–22 (2022).
55. A. Vaks et al., Palaeoclimate evidence of vulnerable permafrost during times of low sea ice. Nature 577, 221–225 (2020).
56. M. Heijmans et al., Tundra vegetation change and impacts on permafrost. Nat. Rev. Earth Environ. 3, 68–84 (2022).
57. M. Sturm et al., Winter biological processes could help convert arctic tundra to shrubland. Bioscience 55, 17–26 (2005).
58. D. Nicolsky, V. Romanovsky, V. Alexeev, D. Lawrence, Improved modeling of permafrost dynamics in a GCM land-surface scheme. Geophys. Res. Lett. 34, L08501 (2007).
59. H. Lee, S. Swenson, A. Slater, D. Lawrence, Effects of excess ground ice on projections of permafrost in a warming climate. Environ. Res. Lett. 9, 124006 (2014).
60. G. Hugelius et al., Estimated stocks of circumpolar permafrost carbon with quantified uncertainty ranges and identified data gaps. Biogeosciences 11, 6573–6593 (2014).
61. F. Cheng et al., Alpine permafrost could account for a quarter of thawed carbon based on Plio-Pleistocene paleoclimate analogue. Nat. Commun. 13, 1329 (2022).
62. Q. Yan et al., Enhanced intensity of global tropical cyclones during the Mid-Pliocene warm period. Proc. Nat. Acad. Sci. U.S.A. 113, 12963–12967 (2016).
63. IPCC, "Summary for policymakers" in Climate Change 2021: The Physical Science Basis. Contribution of Working Group I to the Sixth Assessment Report of the Intergovernmental Panel on Climate Change, V. Masson-Delmotte et al., Eds. (Cambridge University Press, 2021).
64. I. Harris et al., Version 4 of the CRU TS monthly high-resolution gridded multivariate climate dataset. Sci. Data 7, 109 (2020).

65. K. Trenberth *et al.*, Global warming and changes in drought. *Nat. Clim. Change* **4**, 17–22 (2014).
66. Y. Zhu, A tripole winter precipitation change pattern around the Tibetan Plateau in the late 1990s. *Atmos. Ocean. Sci. Lett.* **15**, 100223 (2022).
67. D. Chen, Y. Gao, Y. Zhang, T. Wang, Effects of spring Arctic sea ice on summer drought in the middle and high latitudes of Asia. *Atmos. Ocean. Sci. Lett.* **15**, 100138 (2022).
68. J. Brown, O. Ferrians Jr., J. Heginbottom, E. Melnikov, Circum-arctic map of permafrost and ground-ice conditions, Resources, Circum-Pacific Map Series CP-45, scale 1:10,000,000, 1 sheet (1997).
69. T. Sazonova, V. Romanovsky, J. Walsh, D. Sergueev, Permafrost dynamics in the 20th and 21st centuries along the East Siberian transect. *J. Geophys. Res.* **109**, D01108 (2004).
70. F. Nelson, S. Outcalt, A computational method for prediction and regionalization of permafrost. *Arct. Alp. Res.* **19**, 279–88 (1987).
71. R. Li *et al.*, Simulated response of the active layer thickness of permafrost to climate change. *Atmos. Ocean. Sci. Lett.* **14**, 100007 (2021).
72. D. Guo, H. Wang, Simulation of permafrost and seasonally frozen ground conditions on the Tibetan Plateau, 1981–2010. *J. Geophys. Res. Atmos.* **118**, 5216–5230 (2013).
73. D. Guo, H. Wang, D. Li, A projection of permafrost degradation on the Tibetan Plateau during the 21st century. *J. Geophys. Res. Atmos.* **117**, D05106 (2012), 10.1029/2011JD016545.
74. D. Lawrence, A. Slater, S. Swenson, Simulation of present-day and future permafrost and seasonally frozen ground conditions in CCSM4. *J. Clim.* **25**, 2207–2225 (2012).